

## Examining rhyolite lava flow dynamics through photo-based 3D reconstructions of the 2011–2012 lava flowfield at Cordón-Caulle, Chile



J.I. Farquharson <sup>\*</sup>, M.R. James, H. Tuffen

Lancaster Environment Centre, Lancaster University, Lancaster LA1 1YQ, UK

### ARTICLE INFO

#### Article history:

Received 16 May 2015

Accepted 2 September 2015

Available online 11 September 2015

Editor: G. Chiodini

#### Keywords:

Rhyolite

Lava flow emplacement

Structure-from-motion

Viscosity

3D reconstruction

Puyehue Cordón-Caulle

### ABSTRACT

During the 2011–2012 eruption at Cordón-Caulle, Chile, an extensive rhyolitic flowfield was created (in excess of 0.5 km<sup>3</sup> in volume), affording a unique opportunity to characterise rhyolitic lava advance. In 2012 and 2013, we acquired approximately 2500 digital photographs of active flowfronts on the north and east of the flowfield. These images were processed into three-dimensional point clouds using structure-from-motion and multi-view stereo (SfM–MVS) freeware, from which digital elevation models were derived. Sequential elevation models—separated by intervals of three hours, six days, and one year—were used to reconstruct spatial distributions of lava velocity and depth, and estimate rheological parameters. Three-dimensional reconstructions of flowfronts indicate that lateral extension of the rubby, 'a'a-like flowfield was accompanied by vertical inflation, which differed both spatially and temporally as a function of the underlying topography and localised supply of lava beneath the cooled upper carapace. Compressive processes also drove the formation of extensive surface ridges across the flowfield. Continued evolution of the flowfield resulted in the development of a compound flowfield morphology fed by iterative emplacement of breakout lobes. The thermal evolution of flow units was modelled using a one-dimensional finite difference method, which indicated prolonged residence of magma above its glass transition across the flowfield. We compare the estimated apparent viscosity (1.21–4.03 × 10<sup>10</sup> Pa s) of a breakout lobe, based on its advance rate over a known slope, with plausible lava viscosities from published non-Arrhenian temperature–viscosity models and accounting for crystallinity (~50 vol.%). There is an excellent correspondence between viscosity estimates when the lava temperature is taken to be magmatic, despite the breakout being located >3 km from the vent, and advancing approximately nine months after vent effusion ceased. This indicates the remarkably effective insulation of the lava flow interior, providing scope for significant evolution of rhyolitic flow fields long after effusive activity has ceased.

© 2015 Elsevier B.V. All rights reserved.

### 1. Introduction

Lava flows constitute the primary emplacement mechanism for erupting magmatic products at the surface of the Earth and other planetary bodies. As well as providing valuable information regarding planetary evolution and crust formation, their study is vital for understanding the associated hazard posed to settlements or developments in their proximity (Harris and Rowland, 2001). Lava advance is governed by its rheology, and lava rheology is in turn determined by magma composition, temperature, pressure, crystallinity, and vesicularity, which can differ spatially and temporally during an eruption (e.g. Griffiths, 2000). Constraining rheological properties and emplacement behaviour is thus of use both in the interpretation of extant flows and the forecasting of actively emplacing or future flows.

Processes, timescales, and sequence of lava flow emplacement have been inferred from interpretation of solidified flows (e.g. Fink, 1983; Anderson and Fink, 1992; Anderson et al., 1998; Applegarth et al., 2010a, b), or estimated using numerical (e.g. Young and Wadge, 1990; Favalli et al., 2006; Vicari et al., 2007; Ganci et al., 2012; Spataro et al., 2012), thermo-rheological (e.g. Manley, 1992; Stevenson et al., 2001; Wright et al., 2008), or mechanical (e.g. Christiansen and Lipman, 1966; Ventura, 2001) models. Here we constrain the evolving flow characteristics of an active rhyolitic lava using ground-based remote sensing and emergent image analysis techniques. Remote sensing (RS) methods have often been used in order to observe and monitor flows either to directly study structures and processes (e.g. Fink, 1983; Anderson and Fink, 1992; Guest and Stofan, 2005; Applegarth et al., 2010a; Lev et al., 2012) or to derive digital elevation data subsequently used in analysis or modelling (e.g. James et al., 2006; James et al., 2007; Tarquini and Favalli, 2011; Dietterich et al., 2012; Ebmeier et al., 2012). The ability to construct digital elevation models (DEMs) of sufficient quality over relevant timescales depends in turn on having a suitable RS acquisition strategy (Ebmeier et al., 2012). Recent progress has been made in extracting data from RS images or image sets in order to

\* Corresponding author at: Laboratoire de Déformation des Roches, Géophysique Expérimentale, Institut de Physique de Globe de Strasbourg (UMR 7516 CNRS, Université de Strasbourg/EOST), 5 rue René Descartes, 67084 Strasbourg cedex, France.

E-mail address: [farquharson@unistra.fr](mailto:farquharson@unistra.fr) (J.I. Farquharson).

estimate key dynamic parameters governing lava emplacement (e.g. Harris et al., 2004; James et al., 2007). The capacity to derive rheological data from field-based RS images has a number of advantages over traditional field methods such as penetrometers or shear vanes, which are challenging to operate and provide spatially and temporally limited data due to methodological difficulty or issues with site accessibility (Pinkerton and Sparks, 1978).

The approach used in this study involves a combination of structure-from-motion and multi-view stereo (SfM–MVS) computer vision techniques, which allow the development of three-dimensional (3D) spatial data from photographs collected in the field (e.g. James and Robson, 2012). SfM–MVS has been used to construct terrain models of a variety of volcanic environments (e.g. Kolzenburg et al., submitted for publication), as well as to analyse lava flow (James et al., 2012; Tuffen et al., 2013; James and Robson, 2014) and dome (James and Varley, 2012) processes, and offers significant potential for measuring active volcanic processes. Ground-based imaging provides straightforward acquisition with greater spatial and temporal resolution than most satellite or airborne platforms, and is thus well suited for measurement of rapid surface changes associated with ongoing lava emplacement. RS-derived results may then be used in order to obtain basic rheological data regarding lava flows (such as surface velocities or viscosity), for example using the equation of Jeffreys (1925), which relates flow rate (velocity) of a fluid to its intrinsic properties (e.g. viscosity, density) and external forces acting on the flow (e.g. gravity). Despite being developed to model the two-dimensional laminar flow of water on an incline—requiring the assumption of Newtonian behaviour and well-constrained channel dimensions—the Jeffreys (1925) equation has been commonly used to provide first-order estimates of lava viscosity (among others, Hulme, 1974; Gregg and Fink, 1996, 2000; Chevrel et al., 2013) since first being applied to volcanic processes by Nichols (1939).

The use of Jeffrey's equation—and other models based on Newtonian rheology—implies that there is negligible shear stress acting on a flow if it is not in motion. However, the propensity for cooling lava flows to form a solidified crust overlying viscous lava means that this premise is not necessarily appropriate. Accordingly, rheological models such as the constitutive Herschel–Bulkley relation have been similarly applied to lavas and lava flowfields (e.g. Balmforth et al., 2000; Castruccio et al., 2013, 2014) to account for the potential for nonzero shear stresses (corresponding to a yield strength of the crust or core of a lava). These end-member regimes highlight the contrasting theories of “crust-dominated” or “core-dominated” flow (that is, whether flow advance is governed by the rheology of the interior lava or by a thickening overlying crust). Rhyolitic lavas are often posited to have high-yield strength crusts of significant thickness (e.g. Fink and Fletcher, 1978; Fink, 1980), serving to retard flow rates by imparting shear on the internal lava. By analysing photo-based reconstructions of an advancing rhyolitic lava, in concert with simple rheological and thermal models, we seek to explore the properties governing the emplacement dynamics of a compound high-silica flowfield.

### 1.1. Puyehue Cordón-Caulle

The Puyehue Cordón-Caulle Volcanic Complex (PCCVC) comprises the coalesced edifices of Volcán Puyehue and the Cordón-Caulle fissure system, located at 40.5°S in the Andean Southern Volcanic Zone (SVZ) (Fig. 1a). PCCVC is notable in its production of rhyolitic domes and lavas, particularly within the last 100 ka, with significant lava production in the 1921–22 and 1960–61 eruptions (Lara et al., 2006; Singer et al., 2008). For details on the geological history of PCCVC, and a more comprehensive background to the 2011–12 eruption, the reader is referred to Lara et al. (2006), Silva Parejas et al. (2012), and Castro et al. (2013).

The 2011–12 eruption at Puyehue Cordón-Caulle (PCC) allowed, for the first time, the detailed scientific study of an actively evolving rhyolite flow (Tuffen et al., 2013). A moderate explosive eruption (VEI 4:

Silva Parejas et al., 2012) commenced on 4 June 2011, characterised by an initial Plinian column, ballistic explosions, and pyroclastic jetting (Castro et al., 2013). Lava extrusion was observed from 15 June 2011, emanating from the same vents from which the eruption began, initially at a high flux rate ( $30\text{--}80 \text{ m}^3 \text{ s}^{-1}$ ; Silva Parejas et al., 2012). The source vent, at  $40^\circ 32' \text{ S}, 72^\circ 08' \text{ W}$ , fed an extensive flowfield of volume  $>0.5 \text{ km}^3$ , shown in Fig. 1b, which continued to grow even after effusion ceased in April 2012 (Tuffen et al., 2013).

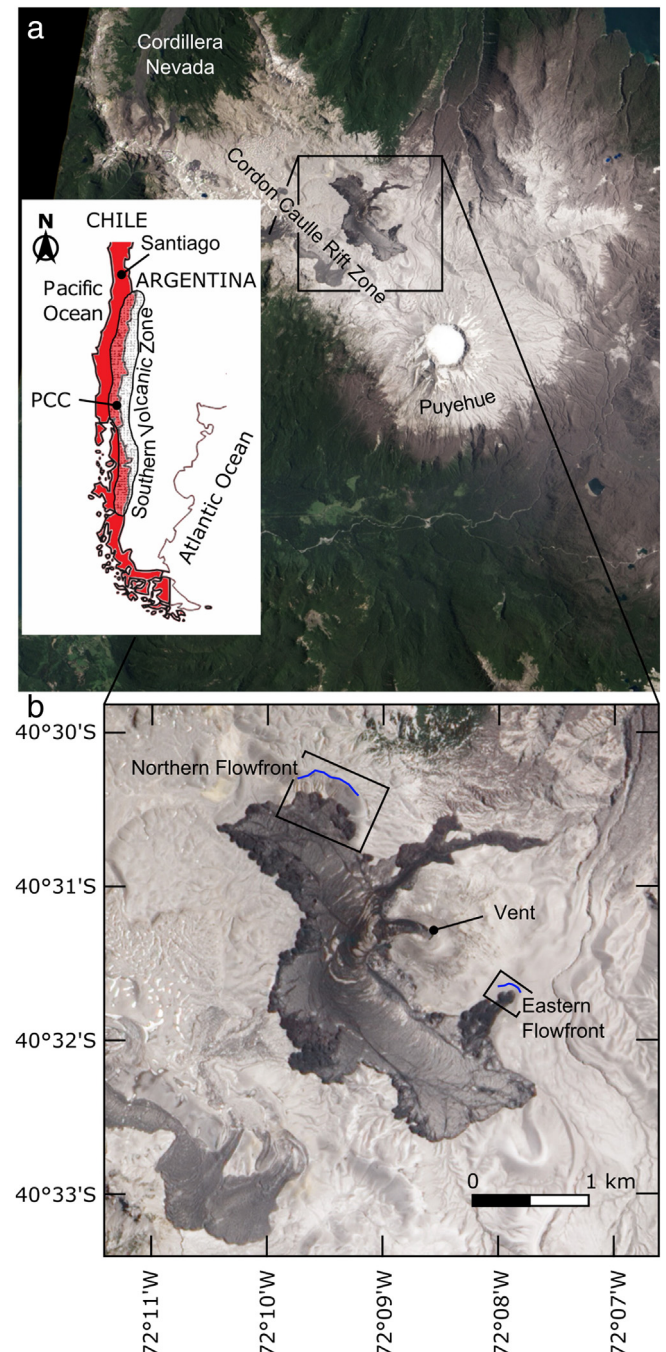


**Fig. 1.** (a) The geographical location of the Puyehue–Cordón Caulle (PCC) Volcanic complex in southern Chile. (b) An aerial image of the Cordón Caulle 2011–2012 lava flow, with the northern and eastern flowfronts indicated with respect to the vent. Blue lines indicate traverse where data acquisition was carried out. (For interpretation of the references to color in this figure legend, the reader is referred to the web version of this article.)

## 1.2. Flow facies

Two main flow surface types can be identified across the flowfield, the first of which comprises rubbly, 'a'a-like lava; approximately 30–45 m thick throughout the areas studied, and typical of most of the flowfield (Tuffen et al., 2013). The upper surface is covered in decimetre- to metre-scale blocks, most of which are roughly equant or subangular (Fig. 2a). The rubbly lava is generally a light grey colour owing to ashfall and vapour-phase precipitates (Tuffen et al., 2013), and a discontinuous pumiceous veneer approximately 0.5 m in thickness (Fig. 2a), with variably oxidised denser lava visible beneath. The margins are bounded by talus, giving the flow a discernible edge between the top and side faces, which assume a generally consistent angle of repose (35–45°). The second surface type is dark grey, brown or black with red oxidised surfaces (Fig. 2b), and formed of larger coherent slabs, spines and tongues of lava, with localised torsion and *en échelon* tensional fractures evident. These two different flow facies are hereafter referred to as rubbly and breakout lava, respectively.

## 1.3. Study areas

During the course of the study, two main regions of the flowfield were investigated, highlighted in Fig. 1b as "northern" and "eastern" flowfronts. The former comprises a number of flow units—both rubbly lobes and breakout units—creating a "scalloped" flow margin

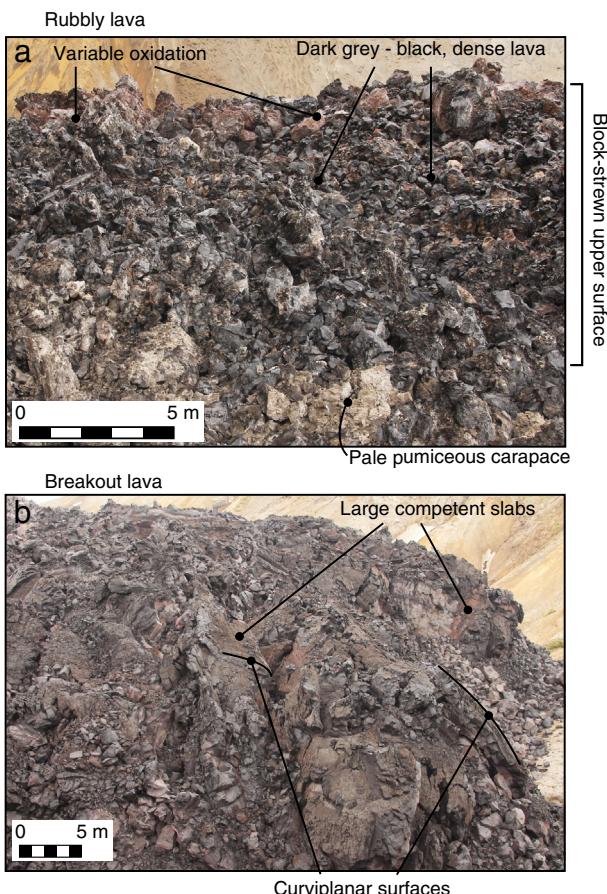


**Fig. 2.** Examples of the two discrete flow facies. Panel (a) shows the block-strewed upper surface of the rubbly lava, looking WSW from 40°30'31.13"S 72°09'37.23"W. Subangular blocks of variably oxidised, dense lava are seen in the background, reaching 2–3 m in diameter. Paler blocks in the foreground have a ~0.5 m-thick pumiceous carapace, which in larger blocks grades into denser, darker lava. In panel (b) the typically slabby upper surface of a breakout consists of larger lava bodies that are several to tens of metres across and bound by curviplanar surfaces. Image looking SE from the same viewpoint as panel (a).

(Figs. 1b; 3a). Constrained by the underlying topography, the majority of this flowfront is abutting against an inward-dipping slope. The eastern flowfront consists of a single unit dominated by a rubbly surface (Fig. 1b, 3b). Crease structures, as described by Anderson and Fink (1992), can be seen at both sites, characterised by metre-scale valleys perpendicular to the flow edge, with convexly sloping walls and an apical angle of between 30 and 90° (e.g. Fig. 3c). On the eastern flowfront, spiny and ensiform structures dominate the upper surface of the flow, as well as large, variably contorted slabs (Fig. 3b, d, e). Endogenous features such as tumuli cannot be discerned at either site.

## 2. Image analysis and 3D reconstruction

Digital field photographs were acquired during 2012 and 2013 during two field campaigns. Initial results using 3D models from the 2012 data (Tuffen et al. 2013) are extended here by modelling thermal structure and rheological properties of the flow from the wider dataset. The northern flowfront was imaged on 04 and 10 January 2012 with a Canon EOS450d digital SLR camera and 28 mm fixed focus lens, from a traverse approximately parallel to the edge of the flowfield, with simultaneous handheld GPS logging of photographer position conducted on the later date. The same site was revisited in January 2013 and a comparable image set collected. The eastern flowfront was imaged twice on 11 January 2013, offset by around three hours, also with synchronous GPS logging. The image suites were processed into 3D point clouds using a SfM-MVS freeware package, as described in James and Robson (2012). SfM-MVS reconstructions require image suites of a given object or scene, with different acquisition positions. Feature-matching algorithms identify prominent features of the scene or object (e.g. Fig. 4a–c) and constructs a sparse (SfM) or dense (MVS) point cloud (e.g. Fig. 4d), with an arbitrary orientation, scale, and geolocation. In this study, derived clouds were filtered using MeshLab processing software, so as to reduce the amount of noise associated with the SfM-MVS approach (e.g. the inclusion of patches of sky).

With the camera clock synchronised to the GPS time, combining the image time-stamps with interpolated GPS logs for the surveys on 10 January 2012 and 11 January 2013 enabled real-world camera coordinates to be estimated for each image. A Matlab tool, sfm\_georef (James and Robson, 2012), was then used to determine a scalar, rotational, and translational transform for the corresponding point clouds using the interpolated camera positions as control data. To register the other datasets to these georeferenced models, sfm\_georef allows the calculation of 3D coordinates of features identified in images. Thus, static features identified in the georeferenced image suites (such as rocks distant from the flow margin) were matched in the unreferenced sets and used as control points to calculate the scaling and georeferencing transform. Data for 04 and 10 January 2012, and January 2013 for the northern study area are hereafter referred to as N<sub>1</sub>, N<sub>2</sub> and N<sub>3</sub>, respectively; data from the first and second traverses of the eastern study area in January 2013 are referred to as E<sub>1</sub> and E<sub>2</sub>. The root-mean-square error (RMSE) between the GPS-derived camera positions and those in the transformed models, N<sub>2</sub> and E<sub>2</sub>, was 4.56 m and 2.06 m respectively. Such values are in line with the expected positional error of the GPS coordinates (Tuffen et al., 2013) and represent the overall uncertainty in absolute geo-referencing. In contrast, the relative registration between sequential 3D models is characterised by RMSE values of 0.22 m (between surveys N<sub>1</sub> and N<sub>2</sub>), 0.21 m (N<sub>2</sub>–N<sub>3</sub>) and 0.09 m (E<sub>1</sub>–E<sub>2</sub>). These relative errors indicate how well the different surveys within the sequences are registered with respect to each other, with their values indicating that sub-metre changes can be detected with confidence.

Flow movement between image acquisition dates was determined by selecting a number of corresponding points on the surface of the lava that are distinguishable in different datasets, enabling 3D displacement vectors to be calculated. Furthermore, selected regions of the

point clouds were interpolated using the kriging method to create DEMs for each of the study areas (e.g. Fig. 4e). Difference maps were calculated for  $N_{1 \rightarrow 2}$ ,  $N_{2 \rightarrow 3}$ , and  $E_{1 \rightarrow 2}$ , by subtracting the earlier surface from the later one in each case.

### 3. Northern flowfront: advance, inflation and breakouts

Effusion rate variations, combined with irregular topography, cooling, and crystallisation, mean that the emplacement of a compound flowfield can be expected to be both spatially and temporally heterogeneous. The difference maps of the northern flowfront (Fig. 5a, b) highlight this: we observe some regions with relatively more inflation than others, and the areas of maximum inflation or advance are not necessarily the same between image suites.

The flow lobes for which a reasonable number of features (twenty or more features, identified in at least nine images) could be matched between 04 and 10 January 2012 are indicated in Fig. 5a. Notably, features associated with a breakout lobe (B1 in Fig. 3a) were estimated to have

moved a mean distance of 11.72 m in the six-day interval, a surface velocity of approximately  $1.95 \text{ m day}^{-1}$ . This is significantly different to that of the rubbly units, which moved at  $0.65$  and  $1.37 \text{ m day}^{-1}$  (R1 and R2, respectively, in Fig. 3a); mean distances of approximately 3.90 and 8.19 m over the same time period. Although the same flow units could be identified in the 2013 dataset ( $N_3$ ), displacement during this time (12 months) had been too great to reliably identify any of the individual features.

The scalloped margin (Fig. 5a, b) is characteristic of compound flowfields: similar morphology can be observed in aerial views of, for example, SP crater in the US, Parícutin (Mexico), or Mt Etna (Italy), indicating iterative emplacement of multiple flow units. Further, the development of surface ridges can be observed, in both time intervals, across the flowfield surface (characterised by inflated arcuate structures and corresponding troughs transverse to the primary flow direction). These ridges are suggestive of compressional processes driven by a thermo-rheological contrast between the relatively hot and viscous lava, and cooler overlying crustal material

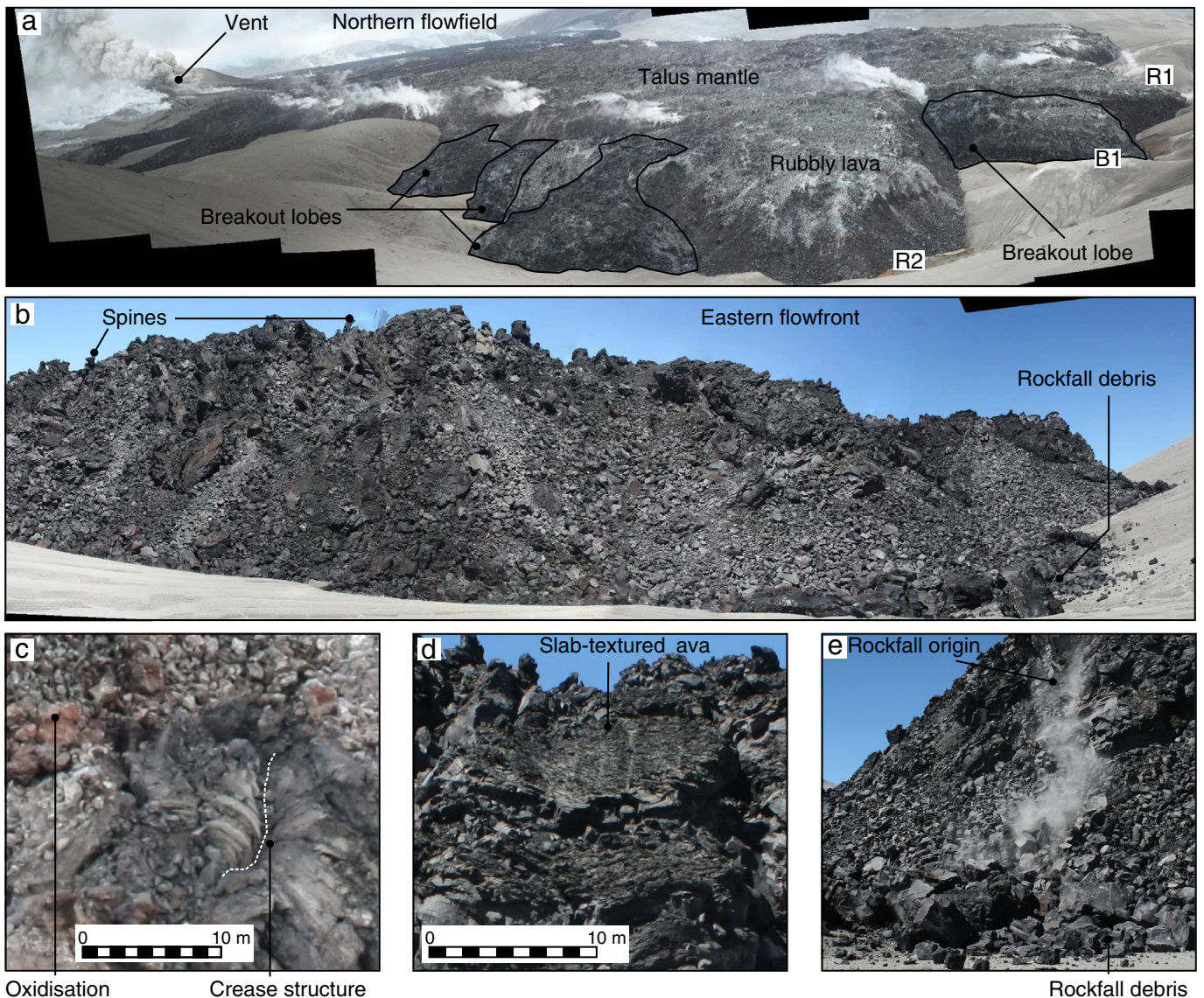


**Fig. 3.** Stitched photo panoramas of the northern and eastern study areas are shown in panels (a) and (b), respectively. The different flow facies—rubbly and breakout lava—are highlighted in panel (a). R1, R2, and B1 refer to two rubbly units and one breakout lobe discussed later in the text. Panel (c) shows a crease structure, in the northern active breakout, as seen on 10 January 2012. Axial valley length (dotted line) is on the order of ten metres. Slab-textured lava is shown in panel (d), on the frontal face of the eastern flowfront. Slab is approximately ten metres in length. Panel (e) is an image captured of an ongoing rockfall from the eastern flowfront. Debris from this and previous rockfalls are shown in both panels (b) and (e).

(Fink and Fletcher, 1978; Fink, 1980). This contrast increases with distance from the vent, causing the upper surface to compress and ruck towards the vent (Lescinsky and Merle, 2005). From a bird's-eye-view, these ridges develop a parabolic form; a result of the flowfield spreading laterally away from the vent, and from a velocity differential between the flow margins and the centre (e.g. Lescinsky and Merle, 2005). The maximum vertical displacement between N<sub>1</sub> and N<sub>2</sub> (from 5 m downwards to 10 m upwards) is probably due to the horizontal translation of these features (Fig. 5a).

Apart from the compressional ridges, inflation is mainly discernible at the front of the rubbly and breakout lobes (Fig. 5a, b), indicating ongoing lava transport to these areas. Between N<sub>2</sub> and N<sub>3</sub> there was no apparent deflation, although some patches remained at a constant thickness over this time. Maximum vertical difference exceeds 40 m over the year; notably, some of the marginal regions that were actively inflating in January 2012 (Fig. 5a) had developed into discrete new breakout units in January 2013 (Fig. 5b). Significant flow inflation and formation of new breakouts in the northern

flowfront is clearly evident from comparing images from 2012 and 2013 (Fig. 6).

The compound morphology of the northern flowfronts indicates that the emplacement was not limited by the supply of lava; an observation supported by ample evidence of flow inflation (Fig. 5). However, whether the advance was retarded by cooling-induced viscosity decrease, or as a result of the variable underlying topography, cannot be determined from the difference maps alone. Existence of multiple lobes means that emplacement was spatially and temporally heterogeneous during and after effusion (nonzero values of surface velocity between 2012 and 2013 datasets prove that flow continued after effusion ceased in April 2012). On a broad scale, the evolution of flow type follows the classification of Lipman and Banks (1987), which categorises flows into a channelised zone, well defined by levees approaching the vent; a dispersed zone, where the flow spreads laterally, and a frontal sector where advance is dominated by "rollover". This classification has been used to describe active basaltic (e.g. Kilburn and Guest, 1993; Bailey et al.,

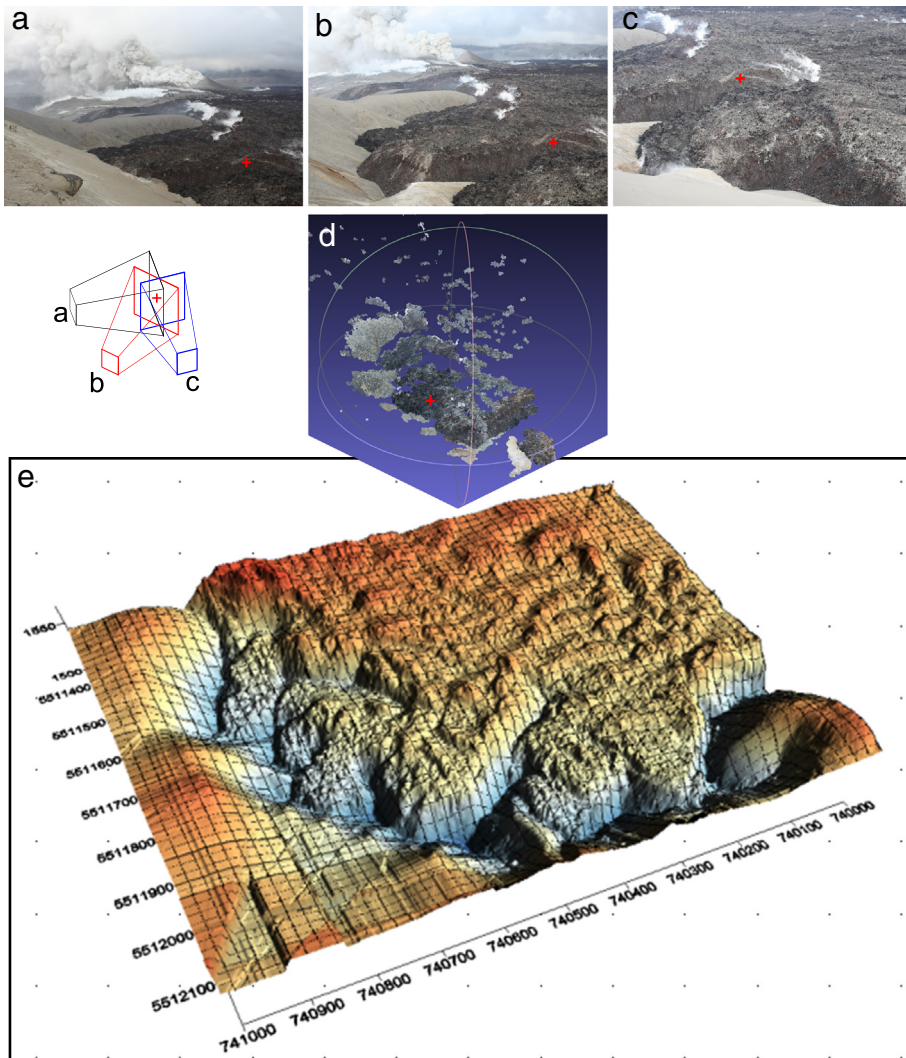


**Fig. 4.** Panels (a) – (c) are examples of images of the flow during the same acquisition campaign, acquired from different viewpoints. Image sets were initially bundled into an unoriented, unscaled mesh cloud, such as panel(d). Once a cloud had been georeferenced, as described in the text, flow features (marked by a red cross in each panel) were identified across separate images and image sets. The georeferenced points were then used to determine a transform for the corresponding points in other image sets (acquisition dates). In practice, a feature had to be discerned in nine or more images in two corresponding sets to be used for the reconstruction and transform. Filtering and interpolating the point cloud data yielded georeferenced DEMs, as shown in panel (e). Refer to text for more details. (For interpretation of the references to color in this figure legend, the reader is referred to the web version of this article.)

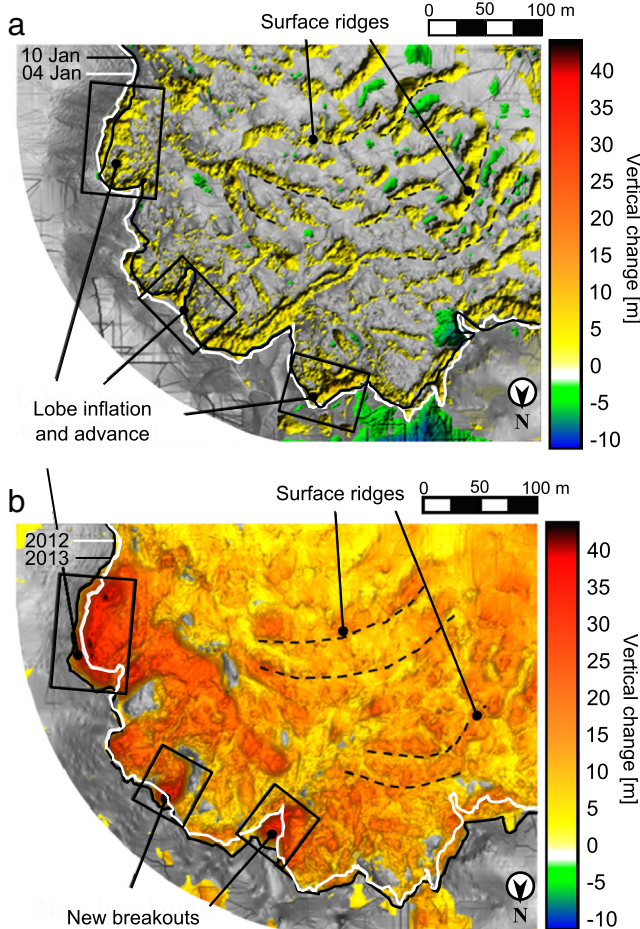


**Fig. 5.** Vertical displacement on the northern flowfront, between N1 and N2 (a): six days between 04 and 10 January 2012, and N2 – N3 and (b): twelve months between 10 January 2012 and 17 January 2013. Horizontal difference (i.e. advance of the flow front) tends to be less than 10 m, whereas vertical displacement (indicated by colour bar) may be up to four times this, in breakout areas. Also shown in (a) and (b) are the flow margins of the corresponding DEMs for each date (given by black and white lines), as well as flow features such as surface ridges and lobe inflation. Vertical displacement is shown by the colour bar, where warm colours are positive (upwards), and cool colours show negative displacement. (For interpretation of the references to color in this figure legend, the reader is referred to the web version of this article.)

2006; Favalli et al., 2010), trachybasetic (e.g. Loock et al., 2010), and dacitic (e.g. Harris et al., 2004) flows.

#### 4. Eastern flowfront: estimating rheological parameters

Naturally, less deformation is observable at the eastern flowfront, due to the much shorter time interval between data acquisition (approximately three hours, rather than days or months). Between image sets E<sub>1</sub> and E<sub>2</sub>, flow features (see Fig. 7a) were displaced a mean distance of 0.26 m over the course of approximately three hours, yielding an average advance rate of 2.10 m day<sup>-1</sup>. However, closer analysis shows that the identified features in the uppermost third of the flowfront generally moved faster and further than those on the lower two thirds (3.08 versus 1.51 m day<sup>-1</sup>, respectively). Fig. 7a distinguishes between the uppermost and lower flow features. Vertical displacement ranges from approximately 7 m upwards to 5 m downwards (Fig. 7b), resulting from flow advance or inflation coupled with rockfall from the top of the flowfront (discernible in the relevant image sets, see Fig. 3e). These observations are

consistent with “caterpillar track” or “rollover” advance typically assumed for ‘a’ā lava flows, whereby cooled and fractured surface material moves to the front of the flow before cascading down the frontal face, eventually forming a contiguous rubble or breccia envelope (e.g. Rowland and Walker, 1987; Kilburn and Guest, 1993; Harris et al., 2004; Lescinsky and Merle, 2005). Analysis of sequential ALI (Advanced Land Imager) images from the NASA EO-1 satellite indicates that the initial advance rate of the eastern flowfront was around 5 m day<sup>-1</sup> (Tuffen et al., 2013); the disparity between these rates is probably due to a combination of topography (discussed and shown in Appendix A, the slope decreases notably in this region), and an overall decrease in volumetric flux supplied to this flowfront over time.

#### 4.1. Estimating viscosity from RS data

As the eastern flowfront approximates a channelised flow moving down an incline, we can complement the RS-derived observations with an estimation of the bulk apparent viscosity  $\eta_A$ , using the Jeffreys (1925) equation:

$$\eta_A = \frac{\rho g d^2 \sin\theta}{nU}. \quad (1)$$

Lava density  $\rho$  is taken as 2300 kg m<sup>-3</sup> (Castro et al., 2013),  $g$  is the acceleration due to gravity (9.81 m s<sup>-2</sup>),  $U$  is the maximum surface velocity ( $3.57 \times 10^{-5}$  m s<sup>-1</sup>), and  $n$  is an empirical constant thus equal to 2 for flow in wide channel. Slope angles  $\theta$  between 2.9 and 7.4° are used, and corresponding flow depths  $d$  between 31.5 and 27.5 m (the derivation of these values is described in Appendix A). For the purpose of this study, viscosity  $\eta$  is considered equivalent to  $\eta_A$  (as in Hulme, 1974; Stevenson et al., 2001; Harris et al., 2004). The derived range of viscosities is between  $1.21 \times 10^{10}$  and  $4.03 \times 10^{10}$  Pa s.

#### 4.2. Post-emplacement flow-cooling

Once emplaced, a lava flow will primarily lose heat to the atmosphere by radiation and convection (Griffiths, 2000), whereas heat transport within the flow is dominated by conduction (Manley, 1992). The Péclet ( $Pe$ ) number defines the ratio of conductive and convective heat transport within the system—i.e. the thermal energy conducted within the lava unit versus the convective transport of heat away from the unit—and is determined by  $Pe = U/\sqrt{dg}$ . The calculated Péclet value for the eastern flowfront is much greater than one ( $Pe = 1113$ ); as such we may reasonably adopt a simple one-dimensional finite cooling model in order to constrain post-emplacement temperature profiles (Patankar, 1980). The model assumes a flow depth of 30 m, and an initial basal temperature equal to the mean of the eruption and basement temperatures (as in Manley, 1992; Stevenson et al., 2001). Eruption temperature is assumed to be 900 °C (Castro et al., 2013). Neglecting the contrasting effects of heat radiation and rainfall-driven advective cooling versus viscous heating, we obtain a first-order estimate of flow cooling over time due to conduction alone. For each timestep, temperature is calculated at nodes every metre into the flow and the underlying basement rock. Boundary conditions are constant, in that the interface between the lava surface and air is 0 °C (consistent with local atmospheric temperatures, given the altitude ~1500 m a.s.l.), as is an arbitrary depth in the basement, which represents an unknown depth at which heat will leave the system (i.e. due to advection due to groundwater). Lava cools by heat conduction over time (e.g. Manley, 1992; Gottsman and Dingwell, 2001). The model is of the form:

$$T_{(i)} = \frac{\kappa \delta t \frac{T_{0(i+1)} - 2T_{0(i)} + T_{0(i-1)}}{\delta z^2} + T_{0(i)}}{1 - \frac{L}{C_P \rho}} + T_{0(i)}; \quad C_P = \frac{k}{\kappa \rho} \quad (2)$$

where  $T_{(i)}$  is the calculated temperature at each vertical node  $i$ ,  $T_0$  is the temperature at the previous timestep, and  $\delta t$  and  $\delta z$  are the intervals for the timestep and vertical node spacing, respectively. Table 1 gives the definition and values of the model parameters.

Consecutive satellite images of the advancing eastern flow (Tuffen et al., 2013) show that the advancing lava in the region was emplaced after 01 November 2013, i.e. in a timeframe  $\leq 74$  days prior to data acquisition. Accordingly, Fig. 8a–g shows the likely temperature profiles through the flow, over time since emplacement. If we assume that the glass transition  $T_g$  of the melt phase occurs at  $10^{12}$  Pa s (Giordano et al., 2008; Hui et al., 2009) then a temperature of around 710 °C can be taken as an approximate threshold for solidification, according to the models of Hess and Dingwell (1996) and Zhang et al. (2003), using glass oxide fractions derived from the eastern flowfront (Schipper et al., 2015). Thus the thickness of the solidified crust of the flow increases with time (shown in Fig. 8). Our model indicates that after a cooling period of two and a half months (Fig. 8b), cooling-induced solidification of the flow has only penetrated the uppermost 2–3 m of the flow at the eastern flowfront. Within the flow, the majority of the rest of the lava remains close to the initial eruption temperature,

being around 830 °C at the base of the flow profile, and near 900 °C in its centre. Thus the solid three metre crust is overlying approximately 27 m of lava still nominally above its glass transition (i.e. able to flow). Our model further indicates that after four years, a 30 m thick rhyolitic lava flow will be entirely below  $T_g$ , and thus completely stalled. Despite this simplified model of flow cooling, other factors can prolong the mobility of the lava (i.e. longer than four years), such as flow down an incline, reactivation of the flow units due to subsurface supply of relatively hotter lava, or reactivation due to flow unit superposition (e.g. Applegarth et al., 2010b).

#### 4.3. Comparing RS-derived viscosities to non-Arrhenian models

In this section, we compare our RS-derived values to those of three published non-Arrhenian temperature–viscosity models (Hess and Dingwell, 1996; Zhang et al., 2003, and Giordano et al., 2008). These models assume a single-phase medium (i.e. melt viscosity only). However, recent work (Schipper et al., 2015) indicates that the crystal fraction of lava from the eastern flowfront is approximately 50 vol.%. Using the modified Einstein–Roscoe equation (e.g. Pinkerton and

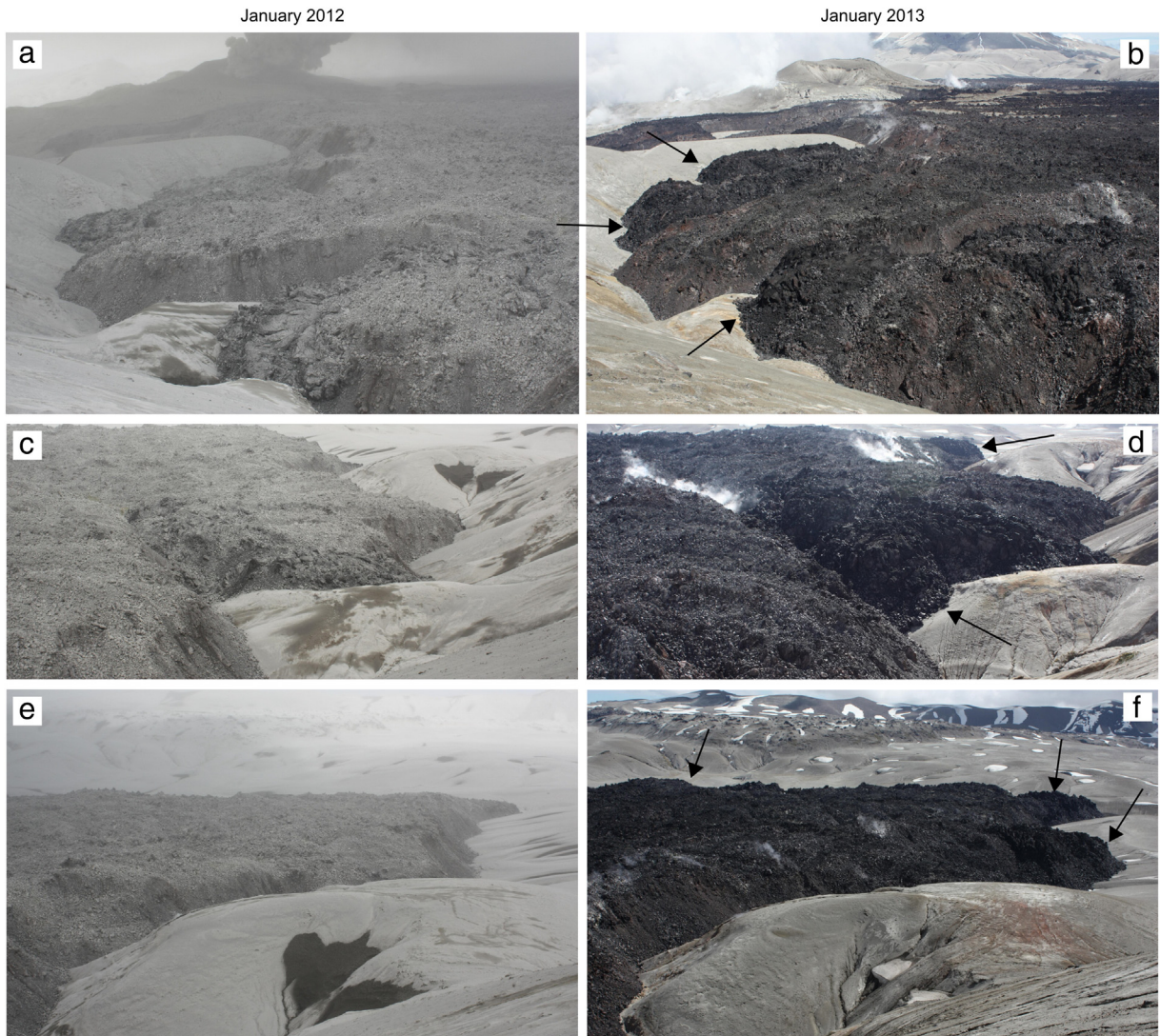


**Fig. 6.** Photographs of the northern flowfront from January 2012 (a, c, e) and January 2013 (b, d, f). Evidence of flow lobe inflation and new breakouts are highlighted by the arrows in the later images.

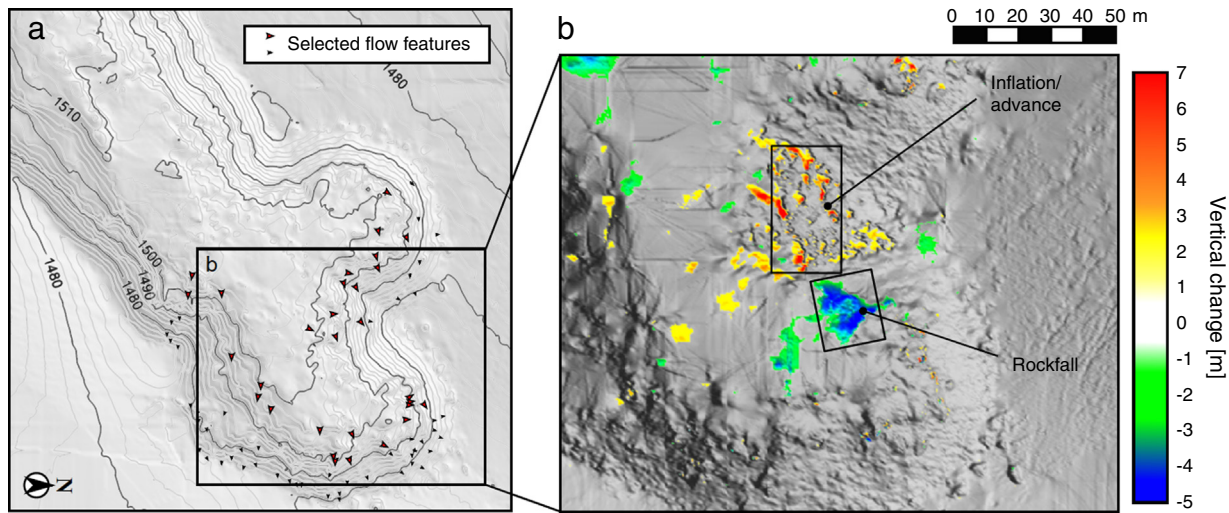


**Fig. 7.** Panel (a) indicates the positions of the matched flow features, superimposed on a reconstructed DEM of the eastern flowfront. Symbols distinguish between those on the upper flow surface (large red arrows) and those on the lower and medial portion of the flowfront (small black arrows). Panel (b) shows vertical displacement on the eastern flowfront, between E1 and E2 (3 h, 11 January 2013 [15:40:50] – [18:27:22]). A region of advance or inflation is indicated, as well as a portion of the flowfront showing predominantly negative displacement (i.e. rockfall). Vertical displacement is shown by the colour bar, where warm colours are positive (upwards), and cool colours show negative displacement. (For interpretation of the references to color in this figure legend, the reader is referred to the web version of this article.)

Stevenson, 1992; Crisp et al., 1994) we can therefore estimate the influence of the crystal fraction  $\phi$  on the effective viscosity of the lava  $\eta$ , whereby

$$\eta = \eta_0(1-R\phi)^{-q} \quad (3)$$

where  $\eta_0$  is the calculated viscosity of the melt (Hess and Dingwell, 1996; Zhang et al., 2003; Giordano et al., 2008), and  $R$  and  $q$  are constants equal to 1.67 and 2.5, respectively. We acknowledge that the Einstein–Roscoe equation is underpinned by some basic assumptions that inherently simplify the influence of crystallisation on lava viscosity. Chief among these is the supposition that crystal growth is isotropic (i.e. spherical), which governs the  $R$  term (Marsh, 1981). The intricacies of the crystal cargo of the PCC lavas—such as the mean aspect ratio and the maximum packing fraction (e.g. Mueller et al., 2010, 2011; Mader et al., 2013; Le Losq et al., 2015)—remain open to a systematic petrographic study. Nonetheless, we observe an excellent coincidence between our estimated range of viscosities (from  $1.21 \times 10^{10}$  to  $4.03 \times 10^{10}$  Pa s) and the modelled ranges (shown in Fig. 9), suggesting that the assumptions are not disproportionate.

## 5. Emplacement summary and implications of the study

Apparent viscosities calculated from emplacement dynamics of the eastern flowfront correspond well with those derived from the models of Hess and Dingwell (1996), Zhang et al. (2003), and Giordano et al. (2008), falling within uncertainty ( $\sim 0.3$  log units of viscosity) in the

same  $T$ - $\eta$  space after accounting for the influence of the crystallinity of the PCC lavas (Fig. 9). This excellent correlation between the RS-derived and modelled viscosities suggests that—despite their simplicity and attendant assumptions—Eqs. (1) and (2) may be used in conjunction to determine a first-order estimate of thermo-rheological properties of advancing silicic lava. Significantly, this implies that, at least in the initial stages of emplacement of any given flow lobe, the advance rate is not notably influenced by an overlying cooled crust. At the time of data acquisition on the eastern flowfront, the degree of cooling had been insufficient to form a surface crust capable of significantly impeding flow advance. This observation agrees with flow textures and breakout emplacement processes modelled using analogues (e.g. by Lescinsky and Merle, 2005).

Crustal control is favoured by long-lived eruptions with relatively low effusion rates, and prolonged cooling of thick lava units (Castruccio et al., 2013). With a longer cooling interval, a high yield-strength crust can develop, increasing in thickness in line with  $\sqrt{kt}$  (Fig. 8). The existence of compressional flow ridges across the northern flowfront attests to this: although the flow interior can retain heat and flow viscously, advance rates are retarded by the thickening crust (Castruccio et al., 2013). The implication that the eastern flowfront initiated as a breakout at (or very close to) the estimated eruption temperature highlights the remarkable insulation of subsurface lava throughout the flowfield. Consistent with Walker's (1971) definition of compound flows, the PCC flowfield is divisible into individual units, with breakout development appearing to be an iterative process whereby new lobes are extruded

**Table 1**

Definition and units of parameters used in Eq. (2) and throughout the text, as well as sources for values pertaining to rhyolitic lava.

Term	Definition	Units	Value and source	
$C_p$	Heat capacity	J kg <sup>-1</sup> K <sup>-1</sup>	1185.8	Eq. (2)
$k$	Thermal conductivity	W m <sup>-1</sup> K <sup>-1</sup>	1.5	Romine et al. (2012)
$L$	Latent heat	J kg <sup>-1</sup>	$5.0 \times 10^5$	Fagents and Greeley (2001)
$\kappa$	Thermal diffusivity	m <sup>2</sup> s <sup>-1</sup>	$5.5 \times 10^{-7}$	Romine et al. (2012)
$\rho$	Bulk density	kg m <sup>-3</sup>	2300	Castro et al. (2013)

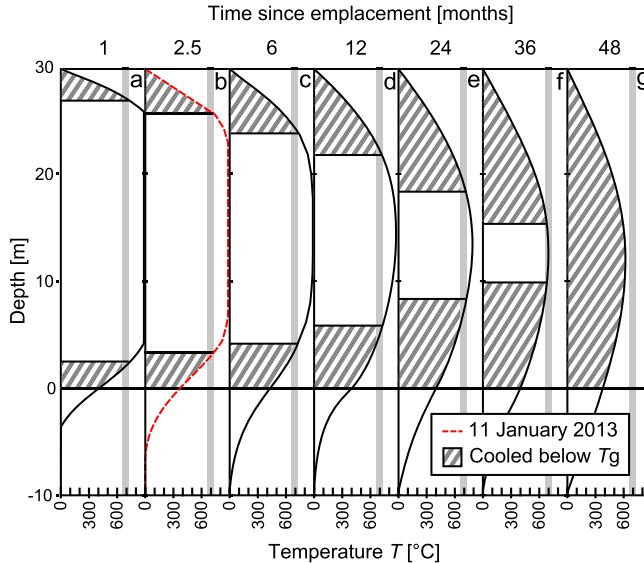


**Fig. 8.** Results of the 1D cooling model Eq. (2). Panels (a) – (g) show temperature profiles for a 30 m thick rhyolite lava 1, 2.5, 6, 12, 24, 36, and 48 months after emplacement, where the grey vertical line represents the potential range of  $T_g$ . The increase in crust thickness over time is illustrated by the hatched regions for each temperature profile. The dashed red line indicates the likely temperature profile for the eastern flowfront at the time of data acquisition, assuming the breakout initiated at or near the eruption temperature (900 °C). Refer to text for full discussion. (For interpretation of the references to color in this figure legend, the reader is referred to the web version of this article.)

viscously and limited in volume by topography and cooling. Those that do persist evolve towards rubbly facies, as the propagation of tensile fractures creates a nascent talus layer (Tuffen et al., 2013). The cooling-driven viscosity increase in the uppermost portion of the flow is reflected in Fig. 8, as predicted by Eq. (2).

The features and inferred emplacement of lava breakouts at PCC have many parallels with those observed at basaltic-intermediate flowfields. For example, blade-like and spiny structures are reminiscent of late-stage lava extrusion in low-silica compound flows, termed “squeeze ups” (Applegarth et al. 2010a). Although transport time between the main and ephemeral vents (i.e. the breakout points) increases as effusion rate dwindles and the flowfield expands, we do not observe a notable increase of cooling and crystallisation of lava in later breakouts (samples from breakouts in 2012 and 2013 both yielded a crystal content of approximately 50 vol.%; Schipper et al., 2015). The observed features generally attributed to significantly higher yield-strength lavas—such as slabby lava (e.g. Guest and Stofan, 2005)—are therefore not necessarily primarily induced by cooling. Rather, it is likely that many of these features arise because of flow stagnation due to the pre-eruption topography of the flowfield, thus increasing the ratio of effusion to advance rate (Guest and Stofan, 2005).

Similarly, the abundance of breakouts at the northern flowfield may be explained by the underlying topography: as the flowfronts in this region abutted against a topographic barrier, the advance rate decreased. Continued supply of lava through subsurface thermal pathways has been discussed with respect to basaltic flowfields (e.g. Calvari and Pinkerton, 1998; Anderson et al., 1999; Guest and Stofan, 2005) and modelled using wax analogues (e.g. Anderson et al., 2005). Interior thermal pathways can apply volumetric stress over large areas of a flow, resulting in spatially extensive inflation and deformation by delivering relatively hotter, less viscous lava to the flowfront or margins (Anderson et al., 2005). A transient or sustained subsurface lava supply to a stagnant lobe can result in overpressure, inflation, and consequent breaching of the solidified crust as a

breakout from an ephemeral vent (Hon et al., 1994); indeed, DEM difference maps (Fig. 5) indicate that breakout emission (e.g. Fig. 6) is typically preceded by a period of inflation. Usually, the precise location of a breakout cannot be predicted, though it is empirically evident that it will be at a point of relatively greater stress: here, difference mapping provides a tool for identifying potential breakout areas. Lava extruded at such a breach will do so initially without a thick crust, as discussed. Until a cooling-induced crust develops on these flow units, breakout lava and the rubbly lava will be subject to distinct shear regimes, reflected in the contrasting surface structures observed in the ‘a’ā and breakout flow facies (Fig. 2). Thus, the governing rheology of silicic lavas may transition from being core-dominated, as inferred for the breakout lobes at PCC, to being controlled by the thickening crust, as we can infer from the compressional processes evident across the flowfield, particularly in the northern study area. This observation is not dissimilar to the frequently observed transition from pāhoehoe to ‘a’ā-type lavas in basaltic systems (e.g. Cashman et al., 1999; Soule et al., 2004). In turn, this supports the inference that flow morphology may be described in a cross-compositional continuum, whereby the evolution of a lava flow or flowfield is a function of the competing influences of internal viscosity (governed by cooling rate, crustal growth, and crystallisation) and advance rate (governed by effusion rate and underlying topography).

Many of the emplacement processes observed at PCC bear similarity to those described for andesitic, dacitic, and basaltic lava flowfields; for example Mt Etna, Italy (e.g. Kilburn and Guest, 1993; Bailey et al., 2006), and Santiaguito, Guatemala (e.g. Harris et al.,

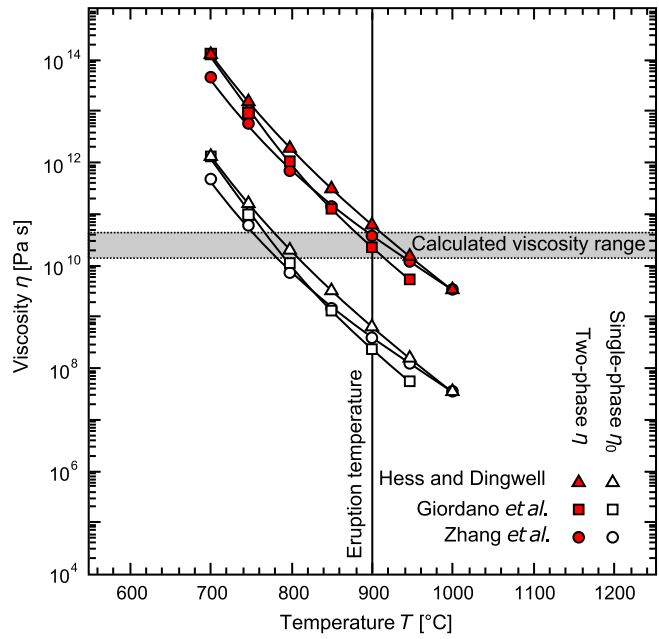


**Fig. 9.** Comparison of RS-derived viscosity range with that predicted by the models of Hess and Dingwell (1996), Zhang et al. (2003), and Giordano et al. (2008) for the eastern flowfront (using glass chemical composition from Schipper et al., 2015). The empty symbols correspond to a single-phase (melt) viscosity  $\eta_0$ , whereas the filled symbols represent a two-phase medium (melt plus crystals)  $\eta$ , as determined using the Einstein–Roscoe equation (Eq. (2)), approximating the effect of 50 vol. % crystals (also taken from Schipper et al., 2015). Grey area delimited by horizontal dotted lines indicates the range of apparent viscosities derived from the RS method (3D reconstruction) via (Eq. (1)); the vertical line gives the likely temperature of interior lava, given a cooling history of 74 days (Eq. (2)) equivalent to the eruption temperature (given by Castro et al., 2013). Refer to text for full discussion. (For interpretation of the references to color in this figure legend, the reader is referred to the web version of this article.)

2004). The existence of cross-compositional features such as crease structures, slabby lava, and breakouts further indicates that compound flow morphology may be described by flow models that encompass rheological differences of many orders of magnitude and suggests the universality of flow models such as those of Walker (1971) or Lipman and Banks (1987). This interpretation is supported by the analogue experiments of Fink and Griffiths (1998). These authors conclude that lava flow morphology evolves sequentially, in a manner dictated by the ratio of cooling and advance rates rather than discrete compositional differences.

Furthermore, as “squeeze-ups” are thought to develop on halted flow units (Applegarth et al., 2010a), the existence of these features on the eastern flowfront highlights that the breakout occurred from a flowfront or lobe that was halted for a time, before being reactivated. We attribute the remarkable mobility calculated for the eastern flowfront to the efficient thermal insulation between the primary vent and the ephemeral breakout vent, after which point it flowed down an incline. This shows that despite low inferred effusion rates and high apparent viscosities, rhyolitic lavas can evolve considerably after initial stagnation, in agreement with Tuffen et al. (2013). This process is facilitated by highly effective heat retention by the brecciated material of the flow surface insulating the hotter and less viscous lava beneath: indeed, our cooling model—though simple—indicates that the innermost portions of the flow could comprise lava hot enough to flow (i.e. above  $T_g$ ), even three years after effusion. In regions of the flowfield where the lava is thicker, this timescale is greatly increased; for example, the model predicts that a lava flow 40 m thick could retain sufficient heat that there would be lava still nominally above the glass transition of its melt phase up to six years after emplacement. Given the degree of displacement we observe in the northern flowfront (Fig. 5a and b) there is ample evidence of lava in the flowfield greater than 40 m in thickness. Thus there remains potential for significant spatial evolution of the flowfield, even years after emplacement.

We suggest that the SfM–MVS techniques could be used to improve flow prediction models by facilitating targeted DEM generation and thus highlighting regions of subsurface supply, inflation and potential hazards. SfM–MVS was found to yield valuable spatiotemporal information over an interval of days to weeks, although useful data were also gained over longer (months) and shorter (hours) timescales. Furthermore, the effects of crystal fraction and surface crust on the apparent viscosity are areas that entreat future research, which may be undertaken by way of scaled analogue models as well as field observation and high-temperature rheological experimentation on lavas.

## 6. Conclusions

Rhyolitic lava flows from the 2011–2012 Cordón-Caulle eruption were found to emplace by processes comparable to those observed in compound flows of less silicic lavas. After an initial period of simple channelised rubbly flow, the lava progressively stagnated, probably primarily due to topographic barriers to flow advance. Lateral extension of the rubbly flowfield was accompanied by spatially and temporally heterogeneous vertical inflation, determined by topography and localised subsurface supply, plus compression and the formation of surface ridges. Continued effusion fed a compound flowfield defined by breakout lobes, some of which matured over time to resemble nascent rubbly units. The apparent viscosity of the last-advancing breakout lobe, as estimated from a simple Newtonian flow model ( $1.21\text{--}4.03 \times 10^{10}$  Pa s), tallies closely with viscosity estimates based on breakout composition. This suggests that, despite advancing nine months after effusion ceased, and >3 km from the vent, this breakout lava remained close to eruption temperatures and was initially governed by internal viscosity, rather than crustal retardation. The highly effective thermal insulation of this rhyolitic lava

yields the potential for significant flowfield evolution—for example breakout initiation, compound flow development, and lateral spreading—even years after the cessation of effusion at the vent. Marked parallels between inferred low- and high-silica processes suggest that compound flow emplacement may be described by universal, cross-compositional models.

## Acknowledgements

JF acknowledges a Lancaster Environment Centre scholarship from Lancaster University. HT was supported by a Royal Society University Research Fellowship. Jon Castro, Ian Schipper and Anne-Marie Militzer are thanked for their logistical help in the field. We thank Dr Magdalena Oryaëlle Chevrel and Prof. Jonathan Fink for their constructive reviews, and Dr Margaret Mangan for handling the manuscript.

## Appendix A. Model parameter estimation

### A.1. Slope

As with any models, the reliability of Jeffreys equation (Eq. (1)) and the cooling model (Eq. (2)) depends on the quality of the input parameters.

In order to constrain the incline angle of the underlying topography at the eastern flowfront, elevation data from prior to the eruption (April 2011) was used. These data were obtained from Google Earth, a free geographical information programme which comprises an amalgamation of elevation data, primarily collected by NASA's Shuttle Radar Topography Mission (SRTM). Fig. A1(a) shows the eastern site pre-eruption. Slope profiles were then extracted with reference to six transects running the length of the eastern flowfront (Fig. A1, c). The elevations corresponding to the start ( $h_{\text{MAX}}$ ) and finish ( $h_{\text{MIN}}$ ) of each transect are given in Table A1, as are the length of each transect and the corresponding slope value, determined by  $\theta = \tan^{-1}((h_{\text{MAX}} - h_{\text{MIN}})/l_T)$ .

**Table A1**  
Slope profile data for the eastern flowfront (pre-eruption).

Path	Maximum elevation $h_{\text{MAX}}$ [m]	Minimum elevation $h_{\text{MIN}}$ [m]	Distance $l_T$ [m]	Slope angle $\theta$ [°]
1	1340	1330	200	2.9
2	1343	1325	250	4.1
3	1348	1327	250	4.8
4	1349	1325	250	5.5
5	1354	1327	250	6.2
6	1360	1334	200	7.4

### A.2. Lava thickness

Accounting for the basal slope and the distance  $l$  between the two points (a and b, Fig. A2) gives us an estimate of the flow depth  $d$ , approximated by  $d = d_T - (\tan \theta l)$ , where  $d_T$  is the total difference between the top and base of the flow (the difference between b and c in Fig. A2). The determined range of flow depths (from 27.5 to 31.5 m) has been incorporated into the thermal and rheological model estimations in the main body of the text (i.e. Eqs. (1) and (2)).

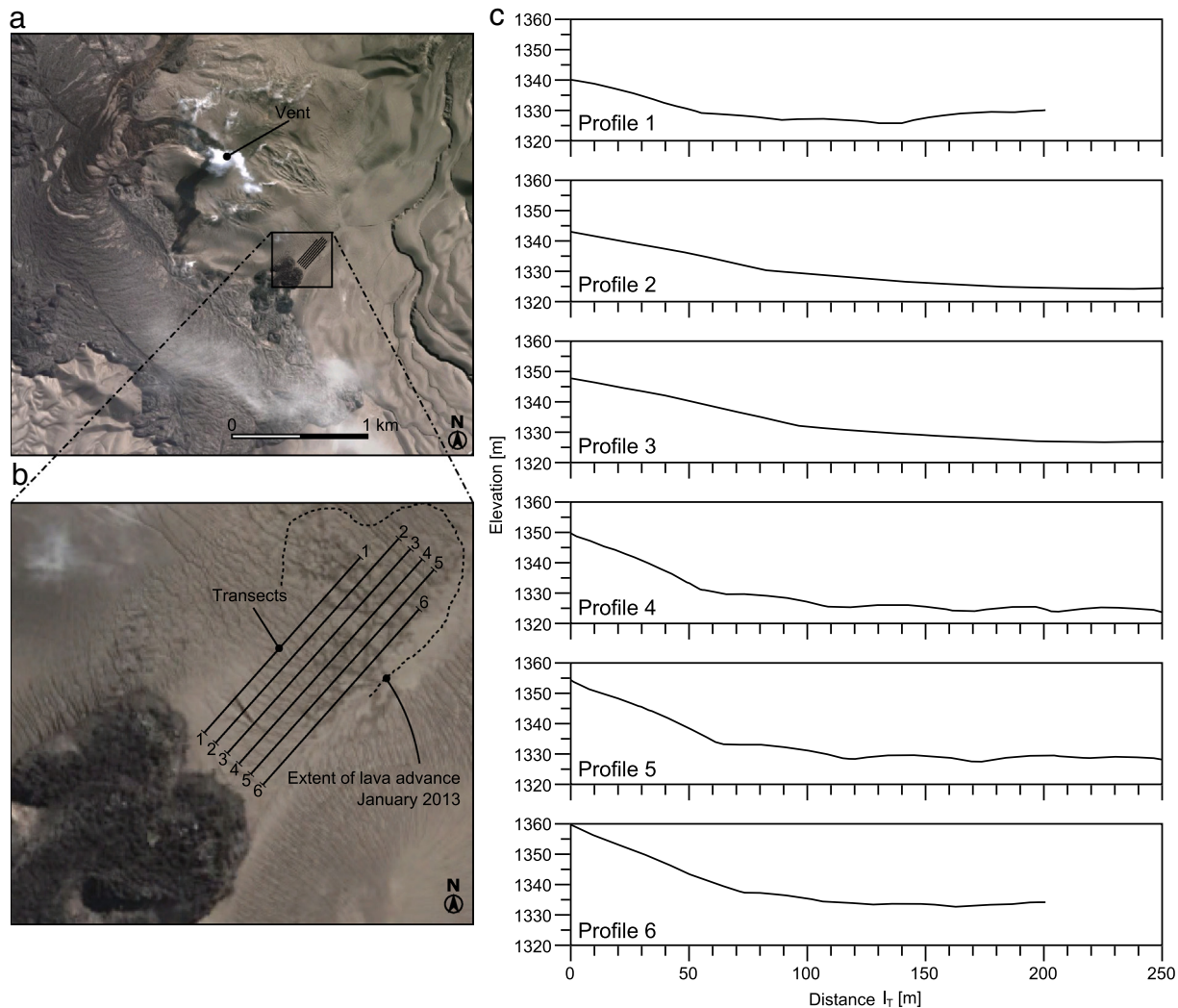


**Fig. A1.** (a) Satellite image of the eastern site, prior to the advance of the eastern flowfront. In the zoomed image (b), the transects 1–6 are shown. Dashed line indicates the extent of lava advance at the time of data acquisition. The individual slope profiles along the length of each transect  $l_T$  are given in (c).

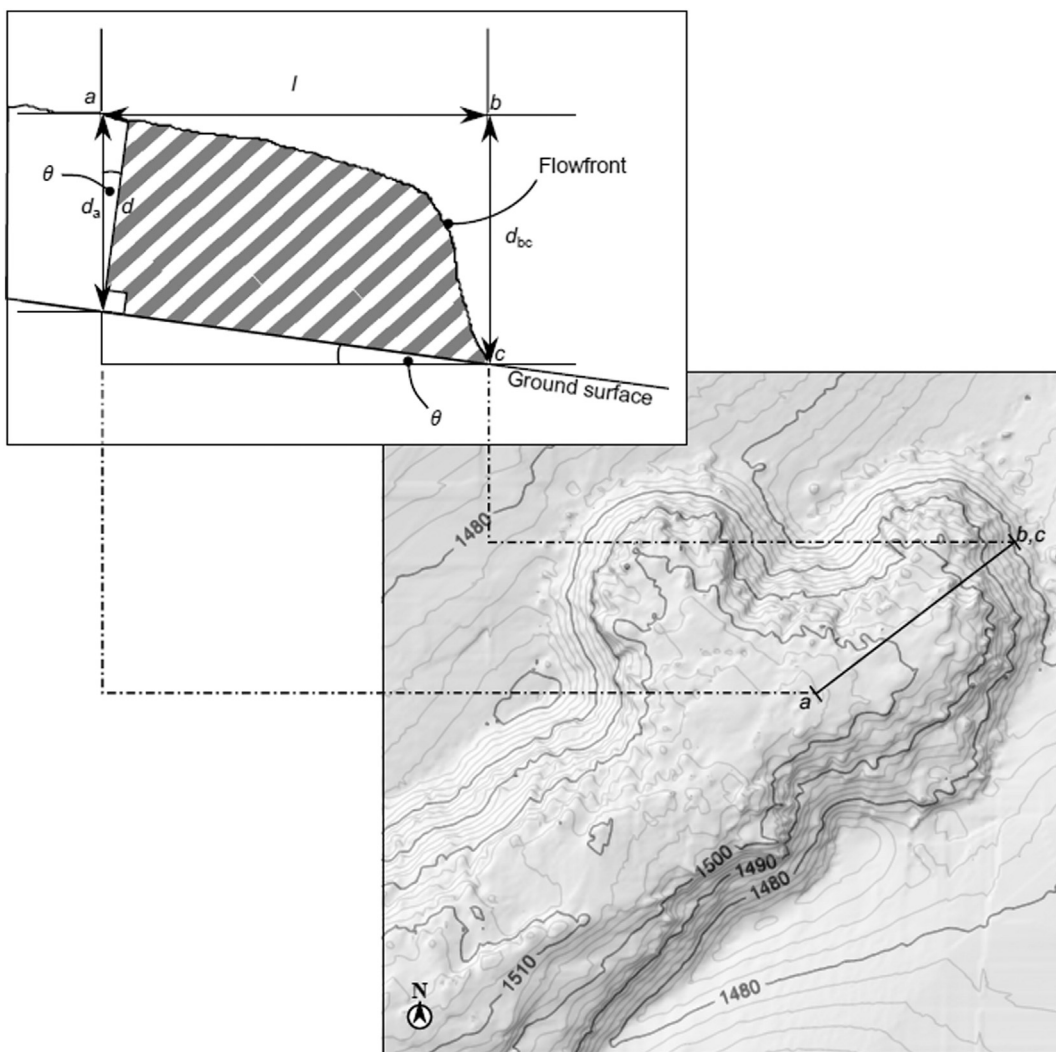


**Fig. A2.** Simplified flowfront geometry used to approximate flow depth  $d$  at the eastern flowfront. The points  $a$  and  $c$  correspond to the top and bottom of the flowfront, respectively. The straight-line distance between them ( $l$ ) is given by the difference between  $a$  and  $b$ , and the total height difference  $d_{bc}$  between the points is determined by  $b-c$ .  $d_a$  is then calculated by accounting for the slope angle, as discussed in the text.

## References

- Anderson, S.W., Fink, J.H., 1992. Crease structures: indicators of emplacement rates and surface stress regimes of lava flows. *Geological Society of America Bulletin* 104 (5), 615–625.
- Anderson, S.W., Stofan, E.R., Plaut, J.J., Crown, D.A., 1998. Block size distributions on silicic lava flow surfaces: implications for emplacement conditions. *Geological Society of America Bulletin* 110 (10), 1258–1267.
- Anderson, S.W., Stofan, E.R., Smrekar, S.E., Guest, J.E., Wood, B., 1999. Pulsed inflation of pahoehoe lava flows: implications for flood basalt emplacement. *Earth and Planetary Science Letters* 168 (1), 7–18.
- Anderson, S.W., McColley, S.M., Fink, J.H., Hudson, R.K., 2005. The development of fluid instabilities and preferred pathways in lava flow interiors: insights from analog experiments and fractal analysis, in kinematics and dynamics of lava flows. In: Manga, M., Ventura, G. (Eds.), *Geological Society of America Special Paper* 39, pp. 148–161.
- Applegarth, L.J., Pinkerton, H., James, M.R., Calvari, S., 2010a. Morphological complexities and hazards during the emplacement of channel-fed 'āā lava flowfields: a study of the 2001 lower flowfield on Etna. *Bulletin of Volcanology* 72 (6), 641–656.
- Applegarth, L.J., Pinkerton, H., James, M.R., Calvari, S., 2010b. Lava flow superposition: the reactivation of flow units in compound 'āā flows. *Journal of Volcanology and Geothermal Research* 194 (4), 100–106.
- Bailey, J.E., Harris, A.J.L., Dehn, J., Calvari, S., Rowland, S.K., 2006. The changing morphology of an open lava channel on Mt. Etna. *Bulletin of Volcanology* 68, 497–515.
- Balmforth, N.J., Burbidge, A.S., Craster, R.V., Salzig, J., Shen, A., 2000. Visco-plastic models of isothermal lava domes. *Journal of Fluid Mechanics* 403, 37–65. <http://dx.doi.org/10.1017/S0022112099006916>.
- Calvari, S., Pinkerton, H., 1998. Formation of lava tubes and extensive flow field during the 1991–1993 eruption of Mount Etna. *Journal of Geophysical Research: Solid Earth* 103 (B11), 27291–27301 1978–2012.
- Cashman, K.V., Thornber, C., Kauahikaua, J.P., 1999. Cooling and crystallization of lava in open channels, and the transition of pāhoehoe lava to 'āā. *Bulletin of Volcanology* 61 (5), 306–323.
- Castro, J.M., Schipper, C.I., Mueller, S.P., Militzer, A.S., Amigo, A., Parejas, C.S., Jacob, D., 2013. Storage and eruption of near-liquidus rhyolite magma at Cordón Caulle, Chile. *Bulletin of Volcanology* 75 (4), 1–17.
- Castruccio, A., Rust, A.C., Sparks, R.S.J., 2013. Evolution of crust- and core-dominated lava flows using scaling analysis. *Bulletin of Volcanology* 75 (1), 1–15.
- Castruccio, A., Rust, A.C., Sparks, R.S.J., 2014. Assessing lava flow evolution from post-eruption field data using Herschel–Bulkley rheology. *Journal of Volcanology and Geothermal Research* 275, 71–84.
- Chevrel, M.O., Platz, T., Hauber, E., Baratoux, D., Lavallée, Y., Dingwell, D.B., 2013. Lava flow rheology: a comparison of morphological and petrological methods. *Earth and Planetary Science Letters* 384, 109–120.
- Christiansen, R.L., Lipman, P.W., 1966. Emplacement and thermal history of a rhyolite lava flow near Forty-mile Canyon, southern Nevada. *Geological Society of America Bulletin* 77 (7), 671–684.
- Crisp, J., Cashman, K.V., Bonini, J.A., Hougen, S.B., Pieri, D.C., 1994. Crystallization history of the 1984 Mauna Loa lava flow. *Journal of Geophysical Research: Solid Earth* 99 (B4), 7177–7198 (1978–2012).
- Ditterich, H.R., Poland, M.P., Schmidt, D.A., Cashman, K.V., Sherrod, D.R., Espinosa, A.T., 2012. Tracking lava flow emplacement on the east rift zone of Kilauea, Hawai'i, with synthetic aperture radar coherence. *Geochemistry, Geophysics, Geosystems* 13 (5).
- Ebmeier, S.K., Biggs, J., Mather, T.A., Elliott, J.R., Wedge, G., Amelung, F., 2012. Measuring large topographic change with InSAR: lava thicknesses, extrusion rate and subsidence rate at Santiaguito volcano, Guatemala. *Earth and Planetary Science Letters* 335, 216–225.
- Fagents, S.A., Greeley, R., 2001. Factors influencing lava-substrate heat transfer and implications for thermomechanical erosion. *Bulletin of Volcanology* 62 (8), 519–532.

- Favalli, M., Chirico, G.D., Papale, P., Pareschi, M.T., Coltellini, M., Lucaya, N., Boschi, E., 2006. Computer simulations of lava flow paths in the town of Goma, Nyiragongo volcano, Democratic Republic of Congo. *Journal of Geophysical Research: Solid Earth* 111 (B6).
- Favalli, M., Harris, A.J., Fornaciai, A., Pareschi, M.T., Mazzarini, F., 2010. The distal segment of Etna's 2001 basaltic lava flow. *Bulletin of Volcanology* 72 (1), 119–127.
- Fink, J., 1980. Surface folding and viscosity of rhyolite flows. *Geology* 8 (5), 250–254.
- Fink, J.H., 1983. Structure and emplacement of a rhyolitic obsidian flow: Little Glass Mountain, Medicine Lake Highland, Northern California. *Geological Society of America Bulletin* 94 (3), 362–380.
- Fink, J.H., Fletcher, R.C., 1978. Ropy pahoehoe: surface folding of a viscous fluid. *Journal of Volcanology and Geothermal Research* 4 (1), 151–170.
- Fink, J.H., Griffiths, R.W., 1998. Morphology, eruption rates, and rheology of lava domes: Insights from laboratory models. *Journal of Geophysical Research* 1073, 527–545.
- Ganci, G., Vicari, A., Cappello, A., Del Negro, C., 2012. An emergent strategy for volcano hazard assessment: from thermal satellite monitoring to lava flow modeling. *Remote Sensing of Environment* 119, 197–207.
- Giordano, D., Russell, J.K., Dingwell, D.B., 2008. Viscosity of magmatic liquids: a model. *Earth and Planetary Science Letters* 271 (1), 123–134.
- Gottsmann, J., Dingwell, D.B., 2001. The cooling of frontal flow ramps: a calorimetric study on the Rocche Rosse rhyolite flow, Lipari, Aeolian Islands, Italy. *Terra Nova* 13 (3), 157–164.
- Gregg, T.K., Fink, J.H., 1996. Quantification of extraterrestrial lava flow effusion rates through laboratory simulations. *Journal of Geophysical Research: Planets* (1991–2012) 101 (E7), 16891–16900.
- Gregg, T.K., Fink, J.H., 2000. A laboratory investigation into the effects of slope on lava flow morphology. *Journal of Volcanology and Geothermal Research* 96 (3), 145–159.
- Griffiths, R.W., 2000. The dynamics of lava flows. *Annual Review of Fluid Mechanics* 32 (1), 477–518.
- Guest, J.E., Stofan, E.R., 2005. The significance of slab-crusted lava flows for understanding controls on flow emplacement at Mount Etna, Sicily. *Journal of Volcanology and Geothermal research* 142, 193–205.
- Harris, A.J., Rowland, S., 2001. FLOWGO: a kinematic thermo-rheological model for lava flowing in a channel. *Bull. Vol.* 63, 20–40.
- Harris, A.J., Flynn, L.P., Matias, O., Rose, W.I., Cornejo, J., 2004. The evolution of an active silicic lava flowfield: an ETM+ perspective. *Journal of Volcanology and Geothermal Research* 135 (1), 147–168.
- Hess, K.U., Dingwell, D.B., 1996. Viscosities of hydrous leucogranitic melts: a non-Arrhenian model. *American Mineralogist* 81, 1297–1300.
- Hon, K., Kauahikaua, J., Denlinger, R., Mackay, K., 1994. Emplacement and inflation of pahoehoe sheet flows: observations and measurements of active lava flows on Kilauea Volcano, Hawaii. *Geological Society of America Bulletin* 106 (3), 351–370.
- Hui, H., Zhang, Y., Xu, Z., Del Gaudio, P., Behrens, H., 2009. Pressure dependence of viscosity of rhyolitic melts. *Geochimica et Cosmochimica Acta* 73 (12), 3680–3693.
- Hulme, G., 1974. The interpretation of lava flow morphology. *Geophysical Journal International* 39 (2), 361–383.
- James, M.R., Robson, S., 2012. Straightforward reconstruction of 3D surfaces and topography with a camera: accuracy and geoscience application. *Journal of Geophysical Research: Earth Surface* 117 (F3).
- James, M.R., Robson, H., 2014. DEM-sequences of active lava flows from ground-based image sequence processing. *ISPRS J. Photogram. Remote Sens.* 97, 160–170. <http://dx.doi.org/10.1016/j.isprsjprs.2014.08.011>.
- James, M.R., Varley, N., 2012. Identification of structural controls in an active lava dome with high resolution DEMs: Volcán de Colima, Mexico. *Geophysical Research Letters* 39 (22).
- James, M.R., Robson, S., Pinkerton, H., Ball, M., 2006. Oblique photogrammetry with visible and thermal images of active lava flows. *Bulletin of Volcanology* 69, 105–108. <http://dx.doi.org/10.1007/s00445-006-0062-9>.
- James, M.R., Pinkerton, H., Robson, S., 2007. Image-based measurement of flux variation in distal regions of active lava flows. *Geochemistry, Geophysics, Geosystems* 8, Q03005. <http://dx.doi.org/10.1029/2006GC001465>.
- James, M.R., Applegarth, L.J., Pinkerton, H., 2012. Lava channel roofing, overflows, breaches and switching: insights from the 2008–2009 eruption of Mt. Etna. *Bulletin of Volcanology* 74 (1), 107–117.
- Jeffreys, H., 1925. The flow of water in an inclined channel of rectangular section. *Philosophical Magazine* 49, 793–807.
- Kilburn, C.R., Guest, J.E., 1993. Aa lavas of Mount Etna, Sicily. In: Kilburn, C.J., Luongo, G. (Eds.), *Active Lavas*. UCL Press, London, pp. 73–106.
- Kolzenburg, S., Favalli, M., Fornaciai, A., Isola, I., Harris, A.J.L., Nannipieri, L., Giordano, D., 2015. Comparison Between Structure From Motion (SfM) and LiDAR 3D Terrain Models: An Application to Volcanic Surfaces Submitted for publication.
- Lara, L.E., Moreno, H., Naranjo, J.A., Matthews, S., Pérez de Arce, C., 2006. Magmatic evolution of the Puyehue–Cordón Caulle volcanic complex (40°S), Southern Andean Volcanic Zone: from shield to unusual rhyolitic fissure volcanism. *Journal of Volcanology and Geothermal Research* 157 (4), 343–366.
- Le Losq, C., Neuville, D.R., Moretti, R., Kyle, P.R., Oppenheimer, C., 2015. Rheology of phonolitic magmas—the case of the Erebus lava lake. *Earth and Planetary Science Letters* 411, 53–61.
- Lescinsky, D.T., Merle, O., 2005. Strain in lava flows and the formation of fractures in surface crust, in kinematics and dynamics of lava flows. In: Manga, M., Ventura, G. (Eds.), *Geological Society of America Special Paper* 396, pp. 163–179.
- Lev, E., Spiegelman, M., Wysocki, R.J., Karson, J.A., 2012. Investigating lava flow rheology using video analysis and numerical flow models. *Journal of Volcanology and Geothermal Research* 247–248, 62–73.
- Lipman, P.W., Banks, N.G., 1987. Aa flow dynamics, Mauna Loa. *U.S. Geological Survey Professional Paper* 1350, 1527–1567.
- Loock, S., De Vries, B.V.W., Hénot, J.M., 2010. Clinker formation in basaltic and trachybasaltic lava flows. *Bulletin of Volcanology* 72 (7), 859–870.
- Mader, H.M., Llewellyn, E.W., Mueller, S.P., 2013. The rheology of two-phase magmas: a review and analysis. *Journal of Volcanology and Geothermal Research* 257, 135–158.
- Manley, C.R., 1992. Extended cooling and viscous flow of large, hot rhyolite lavas: implications of numerical modeling results. *Journal of Volcanology and Geothermal Research* 53 (1), 27–46.
- Marsh, B.D., 1981. On the crystallinity, probability of occurrence, and rheology of lava and magma. *Contribution to Mineralogy and Petrology* 78, 85–98.
- Nichols, R.L., 1939. Viscosity of lava. *The Journal of Geology* 290–302.
- Patankar, S.V., 1980. *Numerical Heat Transfer and Fluid Flow*. McGraw-Hill, New York 0-89116-522-3.
- Pinkerton, H., Sparks, R.S.J., 1978. Field measurements of the rheology of lava. *Nature* 276, 383–385.
- Pinkerton, H., Stevenson, R.J., 1992. Methods of determining the rheological properties of magmas at sub-liquidus temperatures. *Journal of Volcanology and Geothermal Research* 53 (1), 47–66.
- Romine, W.L., Whittington, A.G., Nabelek, P.J., Hofmeister, A.M., 2012. Thermal diffusivity of rhyolitic glasses and melts: effects of temperature, crystals and dissolved water. *Bulletin of Volcanology* 74 (10), 2273–2287.
- Rowland, S.K., Walker, G.P., 1987. Toothpaste lava: characteristics and origin of a lava structural type transitional between pahoehoe and aa. *Bulletin of Volcanology* 49 (4), 631–641.
- Schipper, C.I., Castro, J., Tuffen, H., Wadsworth, F., Chappell, D., Pantoja, A.E., Simpson, M., Le Ru, E.C., 2015. Cristobalite in the 2011–2012 Cordón Caulle eruption (Chile). *Bulletin of Volcanology* 77, 19.
- Silva Parejas, C., Lara, L.E., Bertin, D., Amigo, A., Orozco, G., 2012, April. The 2011–2012 eruption of Cordón Caulle volcano (Southern Andes): evolution, crisis management and current hazards. *EGU General Assembly Conference Abstracts*. 14, p. 9382.
- Singer, B.S., Jicha, B.R., Harper, M.A., Naranjo, J.A., Lara, L.E., Moreno-Roa, H., 2008. Eruptive history, geochronology, and magmatic evolution of the Puyehue–Cordón Caulle volcanic complex, Chile. *Geological Society of America Bulletin* 120 (5–6), 599–618.
- Soule, S.A., Cashman, K.V., Kauahikaua, J.P., 2004. Examining flow emplacement through the surface morphology of three rapidly emplaced, solidified lava flows, Kīlauea Volcano, Hawai'i. *Bulletin of Volcanology* 66 (1), 1–14.
- Spataro, W., Avolio, M.V., Lupiano, V., Trunfio, G.A., Rongo, R., D'Ambrosio, D., 2012. The latest release of the lava flows simulation model SCIARA: first application to Mt Etna (Italy) and solution of the anisotropic flow direction problem on an ideal surface. *Procedia Computer Science* 1 (1), 17–26.
- Stevenson, R.J., Dingwell, D.B., Bagdassarov, N.S., Manley, C.R., 2001. Measurement and implication of "effective" viscosity for rhyolite flow emplacement. *Bulletin of Volcanology* 63 (4), 227–237.
- Tarquini, S., Favalli, M., 2011. Mapping and DOWNFLOW simulation of recent lava flowfields at Mount Etna. *Journal of Volcanology and Geothermal Research* 204 (1), 27–39.
- Tuffen, H., James, M.R., Castro, J.C., Schipper, C.I., 2013. Exceptional mobility of a rhyolitic obsidian flow: observations from Cordón-Caulle, Chile, 2011–2013. *Nature Communications* 4, 2709. <http://dx.doi.org/10.1038/ncomms3709>.
- Ventura, G., 2001. The strain path and emplacement mechanism of lava flows: an example from Salina. *Earth and Planetary Science Letters* 188 (1), 229–240 southern Tyrrhenian Sea, Italy.
- Vicari, A., Alexis, H., Del Negro, C., Coltellini, M., Marsella, M., Projetti, C., 2007. Modeling of the 2001 lava flow at Etna volcano by a cellular automata approach. *Environmental Modelling and Software* 22 (10), 1465–1471.
- Walker, G.P.L., 1971. Compound and simple lava flows and flood basalts. *Bulletin Volcanologique* 35 (3), 579–590.
- Wright, R., Garbeil, H., Harris, A.J., 2008. Using infrared satellite data to drive a thermo-rheological/stochastic lava flow emplacement model: a method for near-real-time volcanic hazard assessment. *Geophysical Research Letters* 35 (19).
- Young, P., Wadge, G., 1990. FLOWFRONT: simulation of a lava flow. *Computers and Geosciences* 16 (8), 1171–1191.
- Zhang, Y., Xu, Z., Liu, Y., 2003. Viscosity of hydrous rhyolitic melts inferred from kinetic experiments, and a new viscosity model. *American Mineralogist* 88 (11–12), 1741–1752.